NASA/TM–2013-000000

Flexible Micropost Arrays for Shear Stress Measurement

Christopher J. Wohl, Frank L. Palmieri, John W. Hopkins, Allen M. Jackson, John W. Connell

Langley Research Center, Hampton, Virginia

Yi Lin

National Institute of Aerospace, Hampton, Virginia

Alexxandra A. Cisotto

NASA Langley Aerospace Research Summer Scholar (LARSS), Langley Research Center, Hampton, Virginia

October 2013

NASA STI Program . . . in Profile

Since its founding, NASA has been dedicated to the advancement of aeronautics and space science. The NASA scientific and technical information (STI) program plays a key part in helping NASA maintain this important role.

The NASA STI program operates under the auspices of the Agency Chief Information Officer. It collects, organizes, provides for archiving, and disseminates NASA's STI. The NASA STI program provides access to the NASA Aeronautics and Space Database and its public interface, the NASA Technical Report Server, thus providing one of the largest collections of aeronautical and space science STI in the world. Results are published in both non-NASA channels and by NASA in the NASA STI Report Series, which includes the following report types:

- TECHNICAL PUBLICATION. Reports of completed research or a major significant phase of research that present the results of NASA Programs and include extensive data or theoretical analysis. Includes compilations of significant scientific and technical data and information deemed to be of continuing reference value. NASA counterpart of peer-reviewed formal professional papers, but having less stringent limitations on manuscript length and extent of graphic presentations.

- TECHNICAL MEMORANDUM. Scientific and technical findings that are preliminary or of specialized interest, e.g., quick release reports, working papers, and bibliographies that contain minimal annotation. Does not contain extensive analysis.

- CONTRACTOR REPORT. Scientific and technical findings by NASA-sponsored contractors and grantees.

- CONFERENCE PUBLICATION. Collected papers from scientific and technical conferences, symposia, seminars, or other meetings sponsored or co-sponsored by NASA.

- SPECIAL PUBLICATION. Scientific, technical, or historical information from NASA programs, projects, and missions, often concerned with subjects having substantial public interest.

- TECHNICAL TRANSLATION. English-language translations of foreign scientific and technical material pertinent to NASA's mission.

Specialized services also include organizing and publishing research results, distributing specialized research announcements and feeds, providing information desk and personal search support, and enabling data exchange services.

For more information about the NASA STI program, see the following:

- Access the NASA STI program home page at *http://www.sti.nasa.gov*
- E-mail your question to help@sti.nasa.gov
- Fax your question to the NASA STI Information Desk at 443-757-5803
- Phone the NASA STI Information Desk at 443-757-5802
- Write to:

  STI Information Desk

  NASA Center for AeroSpace Information

  7115 Standard Drive

  Hanover, MD 21076-1320

NASA/TM–2013-000000

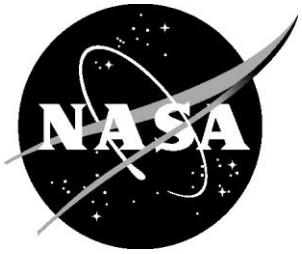

Flexible Micropost Arrays for Shear Stress Measurement

Christopher J. Wohl, Frank L. Palmieri, John W. Hopkins, Allen M. Jackson, John W. Connell

Langley Research Center, Hampton, Virginia

Yi Lin

National Institute of Aerospace, Hampton, Virginia

Alexxandra A. Cisotto

NASA Langley Aerospace Research Summer Scholar (LARSS), Langley Research Center, Hampton, Virginia

National Aeronautics and Space Administration
Langley Research Center Hampton, Virginia 23681-2199

October 2013

National Aeronautics and Space Administration
Langley Research Center Hampton, Virginia 23681-2199

October 2013

Available from:

NASA Center for AeroSpace Information
7115 Standard Drive
Hanover, MD 21076-1320
443-757-5802

Summary:

Significant deficits still exist in the fundamental understanding of boundary layer airflow over subsonic structures, especially regarding drag arising from skin friction. Increased fuel costs, heightened environmental protection requirements, and noise abatement have brought drag reduction to the forefront of aerospace research priorities. Active measurement of shear stress in boundary layer airflow would enable new understanding of how aircraft structure and flight dynamics affect skin friction. This work was focused on developing a shear stress sensor for use in subsonic wind tunnel test facilities applicable to an array of test configurations. The novelty lies in the creation of micropost arrays with a low profile (nanoscale to 100 μm) to stay within the viscous sub-layer of the airflow. Shear stress applied to the micropost causes post deflection and optical property changes. Current shear stress measurement techniques suffer from reliability issues, complex instrumentation, and airflow disruption, severely compromising resultant shear stress data. The state-of-the-art for shear stress sensing uses indirect or direct measurement techniques. Indirect measurements (e.g., hot-wire, heat flux gages, oil interferrometry, laser Doppler anemometry, fences) require intricate knowledge of the studied flow, restrictive instrument arrangements, large surface areas, flow disruption, or seeding material; though smaller, faster probes are currently under development. Direct measurements involve strain displacement of a sensor element and require no prior knowledge of the flow. Unfortunately, conventional "floating" recessed components for direct measurements are mm to cm in size. Whispering gallery mode devices and Fiber Bragg Gratings are examples of recent additions to this type of sensor with much smaller (μm) sensor components. Direct detection techniques, however, are often single point measurements and difficult to calibrate and implement in wind tunnel experiments. Wiring, packaging, and installation of delicate micro-electromechanical devices impede the use of most direct shear sensors. Likewise, the gap required for sensing element displacement is sensitive to particulate obstruction. Additionally, there is a deficit in available instrumentation to adequately characterize acoustic liner efficacy on aircraft engine nacelle walls. **This lack of capability is currently an impediment to research for future applications of these devices on external aircraft surfaces.** Thus, there is a need for a reliable, accurate shear stress sensor with enhanced spatial resolution and simplified installation. Such a measurement device would enable new aerodynamics research needed to design more fuel efficient, quieter aircraft with improved dynamics for smoother and safer flight.

The shear sensors described here would provide a gapless sensor with minimal packaging requirements and minimal or no disturbance of boundary layer flow. Compared to previous concepts, device installation could be simple with reduced cost and down-time. Ultimately, a reliable, accurate shear stress sensor that does not disrupt the airflow has the potential to provide high value data for flow physics researchers, aerodynamicists, and aircraft manufacturers leading to greener, more efficient flight.

Introduction:

Micropillar arrays have been evaluated as sensors for several years. The utility of high aspect ratio structures as environmental sensors has been observed in nature with a variety of functions including

National Aeronautics and Space Administration
Langley Research Center Hampton, Virginia 23681-2199

October 2013

tactile sensing, motion, noise, electrical signals, etc. Researchers have fabricated artificial devices to emulate the efficacy and sensitivity of these natural systems.[1] By natural extension, researchers have investigated the use of these high aspect ratio structures for the measurement of shear forces. State-of-the-art shear stress measurement techniques are often encumbered by the lack of precision, environmental sensitivity, implementation complexity, and in some cases, the requirement of extensive knowledge of the airflow. Naughton and Sheplak[2] and Gad-El Hak[3] have recently reviewed the state-of-the-art for shear stress sensing in wind tunnels. To overcome these challenges, advanced microelectromechanical systems[4] (MEMS) and other promising techniques, including whispering gallery mode sensors[5] and micropillar array devices,[6] are currently being explored.

Brücker, Große, and Schröder have extensively investigated the application of micropillar arrays for shear stress sensing in fluid flows.[7] In their work, micropillars were fabricated via soft lithography from a wax mold template which was patterned using laser ablation.[8] With 300-500 μm tall pillars, they demonstrated deflection of the pillars in fluid flows that were visualized using micro particle image velocimetry (μ-PIV) measurements.[7] The deflection of the pillars was calibrated in a plate and cone rheometer where the experimentally determined deflection was found to correlate well with theoretical calculations. They also evaluated micropillar frequency response and demonstrated the ability to measure both mean[9] and dynamic[10] wall shear stress measurements for water flowing through a circular pipe. Very recently, their micropillar arrays were utilized in wind tunnel to measure shear stress and although there were issues with resonance complications at higher Reynolds numbers, the results indicated that micropillar arrays are amenable to wind tunnel measurements of shear stress.[11]

Several techniques have been demonstrated to efficaciously fabricate high aspect ratio structures. Certainly, other applications for these structures including novel, adhesive free, pressure sensitive adhesives based on Gecko toe topographies[12] and fabrication of superhydrophobic surfaces[13] has contributed to the rapid development of so many fabrication techniques. The most widely used method to generate micropillar structures has been contact lithography followed by a plasma etching[14] or soft lithography.[15] Using this approach, structures with aspect ratios (length/diameter) greater than 10 have been fabricated. Laser ablation patterning to generate templates for soft lithography fabrication has also been demonstrated.[6, 16] More exotic approaches such as growth of nanowire forests and unique tooling were shown to be effective as well for generation of shear sensing pillared surfaces.[17] With such prolific use of these high aspect ratio structures, researchers recently evaluated the stability of them regarding collapse from adhesive and capillary forces identifying requirements for rigidity and pillar spacing.[18] The buckling strength of micropillars, derived from beam theory, has also been investigated.[6] Based on the target pillar dimensions and pillar density for the surfaces fabricated here it is not anticipated that buckling or collapse will be an issue.

In this work, micropillar arrays were generated via soft lithography from templates. The reusable templates were fabricated using either laser ablation patterning or contact lithography. Both unique laser ablation techniques and photomask design for contact lithography were utilized enabling pillars with aspect ratios up to 4 to be reliably produced. The micropillars were fabricated from several

National Aeronautics and Space Administration
Langley Research Center Hampton, Virginia 23681-2199

silicones with varying mechanical properties and characterization of pillar deflection using atomic force microscopy was performed. Thin 'caps' were generated on the tops of the micropillars to be used as aids for deflection sensing. A macroscopic pillar array was fabricated and pillar deflection in a bench top wind tunnel was recording using high speed photography.

Experimental Results:

An elastomeric micropost shear stress sensor was designed to mitigate issues with state-of-the-art techniques. It was important to determine the feasibility of manufacturing the micropost arrays with readily available commercial materials. Several factors were considered in determining the height of the microposts, the spacing of the microposts in the array, and their mechanical properties. In order to remain within the viscous sublayer for subsonic turbulent flows, it was determined that the microposts should not extend significantly beyond 100 micrometers (μm). Similarly, posts should be spaced at least 4 times the diameter of the post 'cap' (see description of pillar capping below) in order to prevent cross-talk between adjacent posts and a cumulative disruption of the airflow properties. Although beam theories are available to accurately describe significant beam deflections, it was decided to target a maximum deflection of 10% of the beam length such that the beam dynamics could be described by classic Euler-Bernoulli beam theory. Using this, the deflection of a cantilever at the tip, y, arising from all forces including form drag and skin friction can be calculated according to:

$$y = \frac{PL^3}{3EI} \tag{1}$$

where E is the modulus, P is the load, and I is the area moment of inertia. Using $P = \tau A$ where A is the area over which the shear force, τ, acts and setting the area equal to half of a cylinder surface area, $A = \pi r(r+L)$, this equation can be rearranged to determine the requisite modulus of the micropillar materials, Eq. 2.

$$E = \frac{40\tau L^2(r+L)}{3r^3} \tag{2}$$

Based on these considerations, calculations were performed to characterize a micropost 100 μm in length and 10 μm in diameter, D, with an elastic modulus of 0.15 MPa (typical elastic modulus of silicones varies from 0.1-3.0 MPa) would undergo deflections of approximately 10% of the pillar length upon shear forces of 10 Pa (Figure 1). Thus, micropillar geometries were determined to be of greatest applicability with L ≤ 100 μm, aspect ratios (L/D) ≥ 5, pillar spacing of 4 times the post 'cap,' and were to be comprised of elastomeric materials with a modulus of ≤ 3 MPa.

National Aeronautics and Space Administration
Langley Research Center Hampton, Virginia 23681-2199

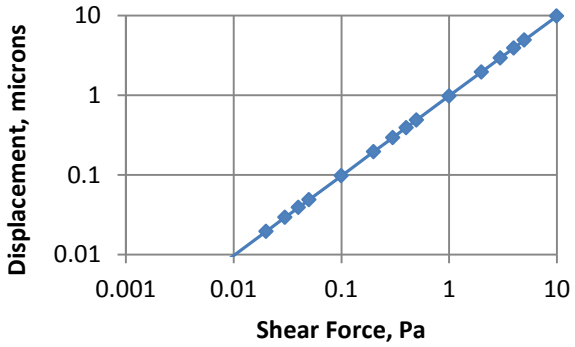

Figure 1. Calculated shear force-displacement curve for a hypothetical pillar 100 μm in length and 10 μm in diameter. The hypothetical pillar had an elastic modulus of 0.15 MPa.

Although these calculations considered the interaction of the micropillars with respect to shear forces, several other forces can play a role in pillar deflection including pressure drag, lift forces normal to the flow vector, inertial forces, and normal pressure forces. The interaction of these forces with micropillars was recently reviewed and their relative contributions to pillar deflection were described.[19] Without an accurate model describing the effects of aerodynamic forces, these sensors must be calibrated in a flow field of known shear force prior to testing unknown flows.

Template Generation via Laser Ablation Patterning

With the target pillar dimensions determined, the optimal laser ablation parameters for master template generation along with what material the master template would be comprised of was determined next. Based on the researchers' experience with laser ablation,[20] it was determined that a polymeric material would be best for use as the master template. A common and readily available 2-part epoxy was investigated as an ablation medium comprised of D.E.R. 331 (Dow) and Ethacure 100 (Albemarle Corporation). Although ablation of the epoxy worked exceptionally well, the resultant ablation depth and ultimate pillar length far exceeded the desired length range (Figure 2A). Therefore, incorporation of an ablation resistant substrate, a material with a greater ablation threshold than the epoxy, was utilized to act as a hard stop. Both silicon wafers and glass disks were evaluated with the glass disks exhibiting better performance as a hard stop. Although laser ablation of the epoxy coupon was too extensive to be a promising path forward, there was a significant amount of information gained about the laser beam profile from this sample (Figure 2B). First, the upper portion of the ablation profile, i.e., closest to the epoxy surface, was much wider than the remainder of the ablated region. Therefore, sacrificial materials were introduced to absorb this portion of the ablation profile. A thick electrical tape (250 μm, 10 mils) was added to the ablation sample lay-up to absorb this energy with a thin layer of wafer dicing tape added between the epoxy

and the electrical tape to assist in sacrificial surface removal upon pattern transcription. Second, the middle portion of the ablation profile had fairly uniform thickness with nearly vertical side walls, i.e., the ablation profile was nearly perpendicular to the epoxy surface. Thus, with the larger portion of the ablation profile consumed in the sacrificial surface and the bottom portion nondestructively absorbed by the silica hard stop, the ablation of the epoxy itself should be relatively uniform. The final configuration for the laser ablation sample layup is shown in Figure 2C. A top-down view of an epoxy sample that was subjected to laser ablation patterning is shown in Figure 2D.

Initially, the laser ablation process involved tracing a small circular area (25.4 μm) on the ablated material. Since the beam diameter is approximately 20 μm, this resulted in features that were 30-40 μm. In an effort to further reduce the feature diameter, a "drill" technique was evaluated. In this technique, instead of having the laser beam translated along a region, the position of the laser beam was fixed and a discrete number of pulses was delivered to the surface. Using this laser drilling approach, the diameters were reduced to approximately 20-30 μm.

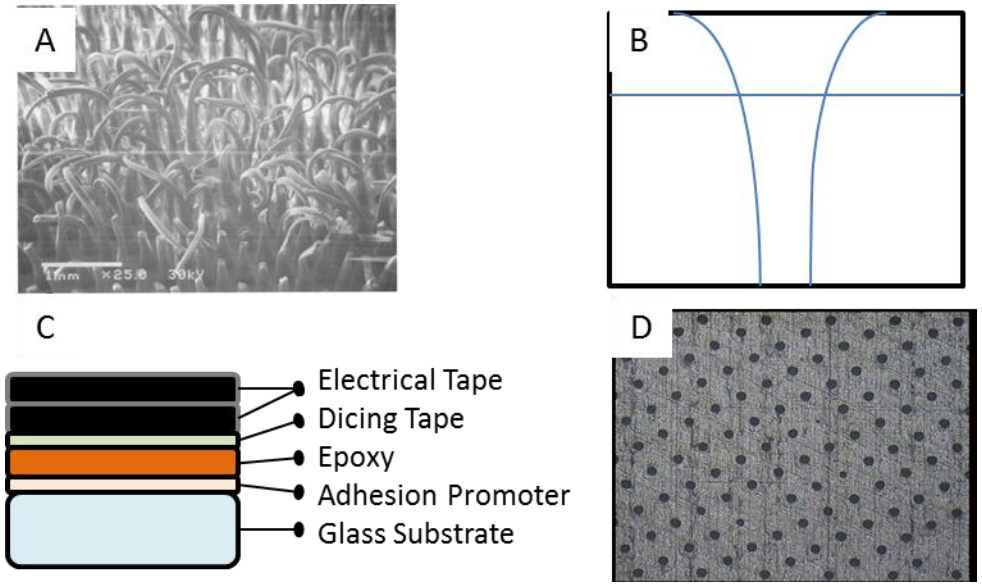

Figure 2. (A) Scanning electron microscope (SEM) image of micropillars generated from laser ablated epoxy coupons. (B) Schematic of the laser beam ablation profile. (C) Current material layup for laser ablation template generation. (D) Top down micrograph of laser ablation patterned epoxy.

Controlling the thickness and planarity of the epoxy is of significance to control the ultimate pillar heights. Several techniques were employed to address the issue of the epoxy "de-wetting" the silica surface after it was spin-cast. Surface oxidation and utilization of adhesion-promoting surface chemical modifiers were investigated with moderate success. A molding technique, which has been successfully demonstrated for controlling bondline thickness in adhesion bonding experiments, was

utilized with significant improvements in surface wetting and epoxy thickness. For this, a glass plate was prepared by solvent cleaning and a small aliquot of the uncured epoxy mixture was placed in the middle. This was surrounded by aluminum alloy shim stock (76.2 μm thick, 3 mils) and the entire surface was covered with a sheet of Teflon and another glass plate. This assembly was placed in a vacuum bag briefly to spread the epoxy, then removed and placed under weights at room temperature for approximately 24 h after which the assembly was placed in a convection oven and stage heated over the course of 72 h to an ultimate cure temperature of 175 °C. This was performed to enable partial curing of the epoxy at low temperatures resulting in an increase in viscosity and preventing uncontrolled flow of the epoxy. Through this process epoxy-coated glass plates have been prepared that are much more planar and have a uniform and consistent thickness of approximately 75 μm.

Another approach to overcome issues with de-wetting of the epoxy on the substrate would be to use an epoxy that cures more rapidly. Along those lines, a 30-minute cure epoxy (Great Plains 30 Minute Pro Epoxy) was utilized to make a series of glass-coated samples. These samples were prepared by placing a small volume (approximately 3 mL) of the mixed 2-part epoxy onto the center of a glass disk that was placed on the spin coater. Several samples were prepared at different spin speeds with a constant duration (60 s) to develop a spin curve (Figure 3).

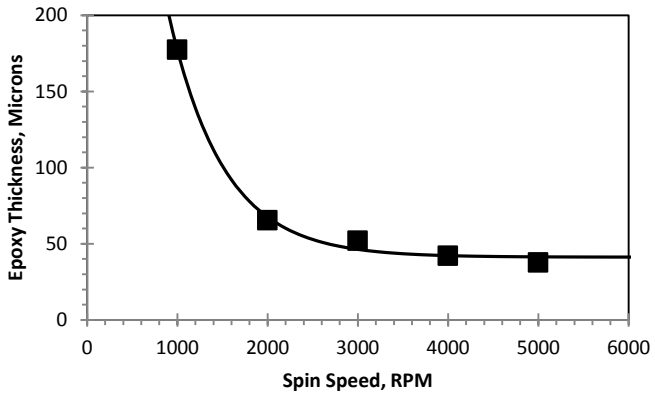

Figure 3. Spin curve developed for the 30 minute cure epoxy deposited on glass slides. The square dots are the data points and the solid line is an exponential fit. The correlation coefficient for this fit was > 0.99.

Using the spin curve in Figure 3, 120 μm thick epoxy-coated glass disks were generated using both a single deposition step and two deposition steps. For the two deposition step process, an initial layer of the epoxy was spin-coated onto the glass disk and placed in a warming oven (70 °C) for 1 hour. This process was repeated to deposit a second epoxy layer on top of the first one. Using the two step process, epoxy thickness variability was reduced from sample to sample relative to the single coating step process.

National Aeronautics and Space Administration
Langley Research Center Hampton, Virginia 23681-2199

Template Generation via Contact Lithography

Another method explored to generate a mask template was to use contact lithography. Silicon wafers were prepared for this process by first removing any surface contaminants or residual organic materials using oxygen plasma exposure. A dehydration bake step was rapidly followed by an adhesion promotion surface chemical modification step. Various surface modification techniques were explored including application of molecular surface modifying agents that would chemically bond to the surface and vapor deposition of copper. Next, a photoresist (SU-8 2050) was applied to the prepared silicon wafer using a syringe. This approach was utilized to prevent introduction of air bubbles into the photoresist which would cause catastrophic surface defects in the final sample. Once applied, the photoresist was spread using a spin coater with an initial spread cycle (500 rpm for 10-15 s) followed by a spin cycle (2500 rpm for 45 s). This ensured that, except for an edge bead which is a typical artifact of this deposition process, the photoresist coated the entire surface in a uniform layer that was approximately 50 μm thick. A soft bake step, involving placing the prepared wafer on a room temperature hot plate and ramping the temperature up to 95 °C over the course of 40 minutes, was used to remove residual solvent. Next, the surface was patterned using a photomask and UV light. Hard contact between the photoresist and the photomask has been demonstrated to be extremely important for consistent pattern transcription and early experiments were unsuccessful due to unforeseen complications with contact (Figure 4A). However, using a vacuum chuck and a long pass filter resulted in excellent pattern transcription after 200 mJ of UV exposure. A hard bake process was performed next involving brief exposure to a 65 °C hot plate (1 minute), a 95 °C hot plate (7 minutes), returning to the 65 °C hot plate (1 minute), and finally, allowing the sample to cool on a nonmetallic surface for 15 minutes. The unexposed photoresist, regions that were under the chromium portions of the photomask and therefore not cross-linked, was removed by submerging the silicon wafer in propylene glycol methyl ether acetate (PGMEA) for 2 minutes. The resultant master template consisted of a silicon wafer with approximately 50 μm of patterned SU-8 photoresist (Figure 4B). Often, due to interfacial stresses, the cross-linked photoresist would delaminate from the surface of the wafer. To mitigate this, a new photomask was designed to generate trenches separating holes of various spacing and array layouts (Figure 4C). The trenches reduced the tensile stress generated in the photoresist during the post exposure bake resulting in a more stable film. Each of the 9 large regions in Figure 3C have a different size and spacing between circular mask features correlating with an ultimate difference in pillar diameter and spacing.

National Aeronautics and Space Administration
Langley Research Center Hampton, Virginia 23681-2199

October 2013

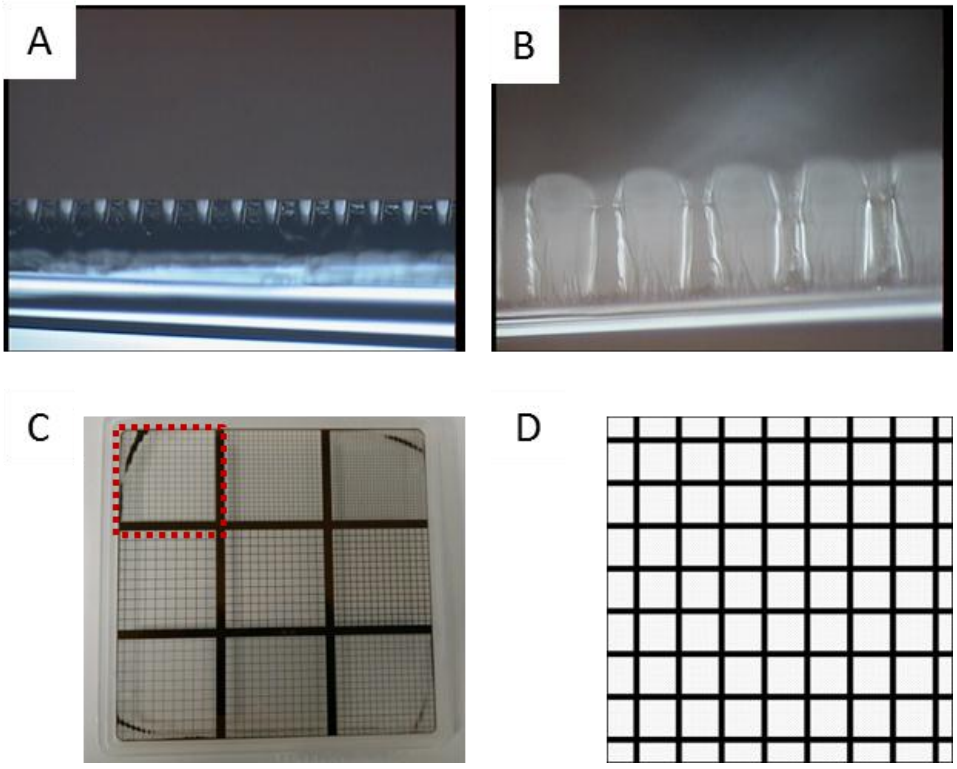

Figure 4. (A) Poor pattern transcription resulting in loss of template fidelity. (B) Better pattern transcription arising from improved contact with the lithography mask. (C) Macroscopic view of new photomask with large lines between patterned regions. (D) Schematic of the region outlined by the dashed line in (C) indicating the smaller lines between regions. Within each 2 mm cell is an array of circular features that are approximately 10 μm in diameter separated by 60 μm.

Micropillar Fabrication

Once the master templates were generated using either laser ablation patterning or contact lithography, the next step was to fabricate the micropost arrays using soft lithography. Several silicone-based materials were evaluated for micropost array generation with a majority of the samples generated using Silastic T2 (Dow-Corning). This flexible, chemically inert, durable silicone is used for a myriad of applications and has excellent environmental durability properties. Additionally, as it is a 2 part silicone, the ratio of the two components (typically 10:1 base:hardener) can be varied resulting in changes in the mechanical properties of the resultant material. Likewise, Sylgard 184 (Dow-Corning) has also been used extensively and was evaluated in this work as low elastic modulus alternative to Silastic T2. To generate the micropost arrays from the master templates, the two part silicone was mixed and spread over the patterned region. This was placed in a vacuum chamber and held under reduced pressure for an hour to enable wetting of the topographical features and removal of trapped air pockets. The silicone was cured at 70 °C for approximately 4 h and allowed to cool to room temperature before removal from the template. In

most instances, the micropillars were readily separated from the template; however, with initial epoxy templates having such deep holes, approximately 40% of the resultant silicone micropillars were fractured upon removal from the template. As these pillars were significantly longer than the desired pillar length which could have contributed to their fracture upon removal, it was not anticipated that this would be an issue in future work. Excellent silicone micropillars were generated from templates prepared using either laser ablation (Figure 5A) or contact lithography (Figure 5B) when the templates had appropriately sized features in them.

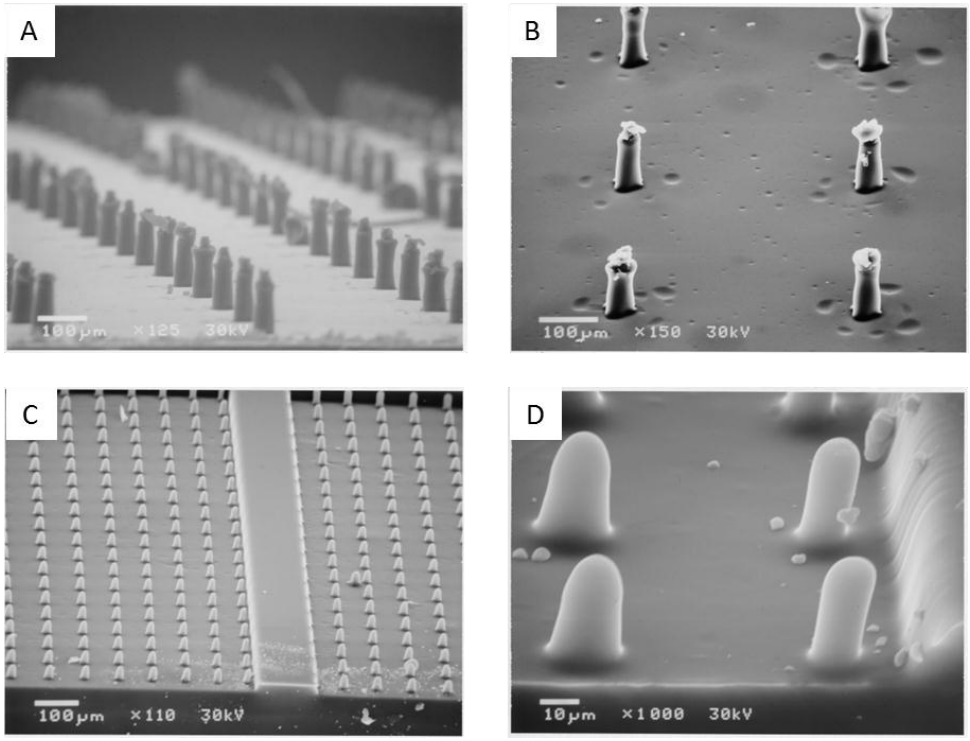

Figure 5. Silastic T2 micropillars generated from a (A and B) laser ablation prepared template and a (C and D) contact lithography prepared template.

Several other silicone materials were evaluated regarding their efficacy towards fabrication of micropost arrays via soft lithography (Table 1). Each of the 2 part silicones were mixed according to the manufacturers' instructions. With the variation in modulus for these materials, from 0.06 MPa to 1.84 MPa, micropillar arrays made from these materials would likely be applicable to a variety of wind speeds and flow conditions. For most materials evaluated the micropillars were readily removed from the templates and resulted in uniform arrays. However, the Sylgard 184 and Solaris A-15 both exhibited a propensity to tearing which made removal difficult. It is possible that changing the ratio of the silicone to hardener for these materials would alleviate these issues but that was not investigated in this work.

National Aeronautics and Space Administration
Langley Research Center Hampton, Virginia 23681-2199

October 2013

Table 1. Mechanical properties and pillar fabrication results for the silicone materials evaluated in this work.

Silicone	Modulus, MPa	Tensile Strength, MPa	Micropillar Fabrication
Sylgard 184[a]	1.84	7.07	✓[c]
Silastic T2	1.50	5.52	✓
Moldstar 30[b]	0.66	2.90	✓
Solaris A-15[b]	0.17	1.24	x[c]
EcoFlex 0050[b]	0.08	2.14	✓
EcoFlex 0010[b]	0.06	0.83	✓

[a]Dow Corning
[b]Smooth-On, Inc.
[c]These silicones were brittle and difficult to work with for this application.

Ultimately, the micropillar design involves the incorporation of a "cap" on top of the pillars. This cap will enable greater deflection resolution by increasing the optical detection area and is anticipated to improve the sensitivity of the pillars. Two important but separate investigations were undertaken with respect to the pillar caps, identification of parameters necessary to make a cap of sufficient thickness and detection enhancement via doping the pillar cap with fluorescent moieties. Micropillar caps were prepared by wetting the pillar tip with uncured silicone followed by cap shaping and silicone curing on a clean surface (Figure 6).

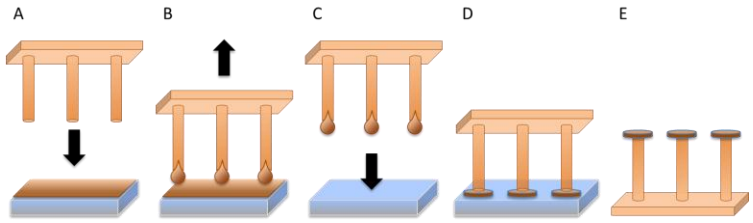

Figure 6. Schematic for fabricating caps on the pillar tips. In this process a micropillar array is placed in contact with a glass substrate coated with a spin-coated uncured silicone layer (A). The micropillar array is removed from this surface leaving microdroplets of uncured silicone on the pillar tips (B) and is brought into contact with a clean glass substrate (C). The uncured silicone partially wets the micropost and partially wets the substrate resulting in formation of circular structures (D) that, once cured, can be removed from the substrate remaining bound to the micropillar tips (E).

National Aeronautics and Space Administration
Langley Research Center Hampton, Virginia 23681-2199

October 2013

Thickness of the uncured silicone film was controlled by spin casting after calibration to prepare a spin curve. Shown below is a representative spin curve generated for Sylgard 184 (Figure 7A), which was chosen due to its reduced viscosity relative to Silastic T2. Using this information, proper surface preparation techniques could be performed to generate a Sylgard 184 coated surface with an appropriate thickness (5-15 μm). Once prepared, a supported silicone micropillar array was carefully brought into contact with the surface and removed resulting in transfer of uncured Sylgard 184 material to the tips of the silicone micropillars. The wetted micropillars were next placed in contact with a clean surface resulting in spreading of the uncured silicone and formation of the micropillar cap. While in contact with the clean surface, the capped micropillars were placed in a 70 °C oven to cure the cap material. The resultant pillars are shown below (Figure 7B). To demonstrate the feasibility to filter the signals detected from the cap movement relative to reflection from the substrate, Silastic T2 was doped with rhodamine B, a fluorescent laser dye. Upon illumination with a UV light source, the fluorescent emission from the doped silicone was readily visible on our macroscopic pillar sample, see below (Figure 7C). This approach will be used to improve signal to noise ratios in actual sensor systems and is amenable to using excitation sources commonly available in wind tunnels (i.e., Nd:YAG lasers, λ=532 nm).

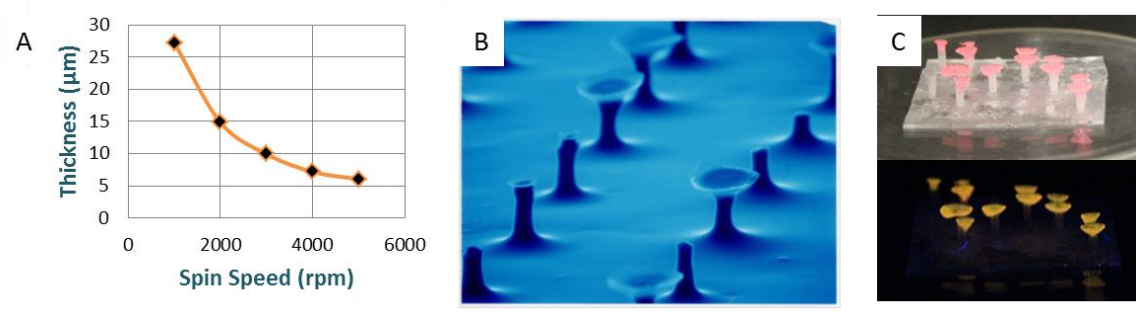

Figure 7. (A) Spin curve for Sylgard 184 with a duration of 30 seconds. (B) SEM image of a preliminary attempt to cap silicone micropillars. (C) Silastic T2 doped with rhodamine B shown as "caps" on the macroscopic shear sensor, described below, under ambient light (top) and UV light (bottom).

Mechanical Characterization of Micropillar Deflection

Once repeatable micropillar arrays were fabricated, experiments were conducted to characterize the mechanical properties of the micropillars using atomic force microscopy (AFM). Based on existing literature, three techniques were investigated for this non-traditional use of AFM equipment. One technique involving contact mode scanning of a pillar decorated surface was quickly excluded as the target heights of the pillar were too great for this approach to be viable.[21] The other two techniques collect force/displacement curves on the pillars as they are bent by the AFM cantilever. Although somewhat similar, one technique involved bending the cantilever down by placing the pillar on top of the cantilever[22] and the other technique involved bending the pillar down by moving the cantilever in that direction.[23] Ultimately, the last technique was chosen due to the instrumentation

available. For these measurements a Veeco Digital Instruments Multimode Scanning Probe Microscope with a Nanoscope V Controller was used. The probes used were MicroMasch cantilevers, CSC12 Tip E with an aluminum coated detector side. The manufacturer data indicated that the average spring constant was k=0.03 N/m. For this technique, cantilevers acquired previously were first calibrated to determine an accurate spring constant. This was achieved by determining fundamental vibrational frequencies for three vibrational modes (bending, lateral, and torsional) using an oscilloscope.[24] Next, the cantilever was placed in contact with the pillar at a determined distance from the base and translated down to deflect the pillar. The deflection of the cantilever was used to calculate the requisite force for pillar deflection using a simple relationship. An example of a pillar that was interrogated using this technique is shown below (Figure 8). Figures 8B, 8C, and 8D show the orientation of the cantilever at three different positions on the pillar prior to pillar bending.

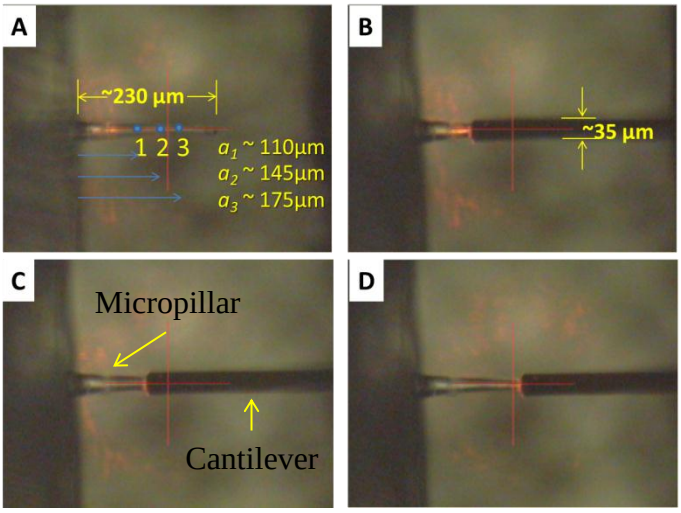

Figure 8. Microscope images of (A) the silicone micropillar interrogated via AFM with the 3 contact points indicated. The AFM cantilever orientation for points 1, 2, and 3 are shown in images B, C, and D, respectively.

Upon bending the pillar, the deflection of the cantilever was recorded which was used to calculate the required force to bend the pillar. An example of the data collected on the pillar shown in Figure 8 is reported here (Figure 9A). As the cantilever was translated downward, it first contacted the micropillar and further movement of the cantilever, resulting in pillar bending, required additional force which was recorded as the deflection force in Figure 9A. As would be anticipated, the deflection force was greater as the cantilever was brought closer to the pillar base as would be anticipated. Initially, the data collected at all 3 pillar locations was collinear which was thought to be due to embedding of the cantilever tip into the silicone itself. Actual deflection of the cantilever is therefore expected to occur where the data differentiates according to the cantilever position, approximately 0.6 µm. One plausible method to circumvent this issue would be to use tipless

cantilevers although that was not investigated in this work. Collection along multiple points of the micropillar surface is important due to the change in velocity, *U(z)*, along the micropillar profile (Figure 9B). This change in velocity is directly related to a change in shear force according to Eq. 3:

$$\tau = \mu \frac{\delta U}{\delta z} \tag{3}$$

where μ is the kinematic viscosity and *z* is the distance from the wall (surface). Thus, experimentally determined deflections of the micropillars in flow fields can be compared to profiles of the deflection force generated using AFM.

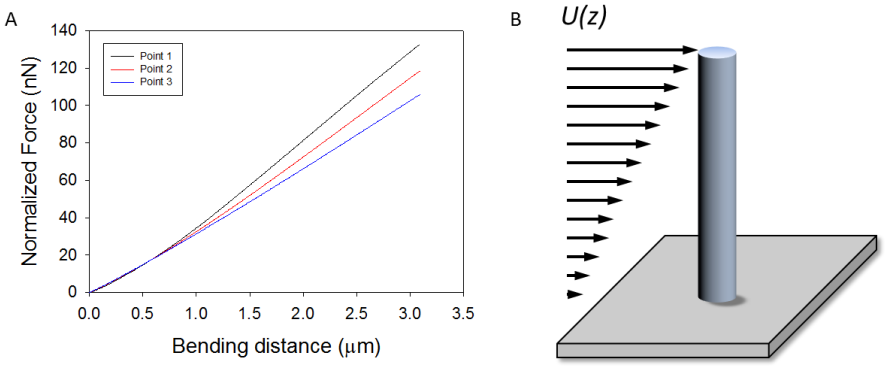

Figure 9. (A) Force deflection curve measured on the pillar shown in Figure 8. (B) Schematic of the change in velocity along the profile of a micropillar in a fluid flow with a no-slip condition.

Deflection forces measured using this AFM technique were related to drag forces experienced in fluid flows using the Oseen approximation.[25] The relative magnitude of shear force present in a uniform Stokes flow resulting in deflection of the micropillar was calculated with the assumption that the force was equivalent to that experienced by an infinitely long cylinder. [See Appendix A for a description of this calculation] Based on the AFM experiments, 3 μm deflection (which was approximately 1.2% deflection relative to the pillar length) resulted in shear forces of approximately 820 mPa (Table 2). Other relationships between deflection force and shear force are included. Thus a shear force of approximately 2 Pa would result in a 10% deflection.

Table 2. Mechanical properties and pillar fabrication results for the silicone materials evaluated in this work.

Force (nN)	τ (mPa)
100	823
50	517
10	176
5	112

Macropillar Demonstration Article Fabrication and Deflection Visualization

To demonstrate the efficacy of this technique, a macroscopic example of the post array was fabricated and high speed photography of pillar deflections was collected. The macroscopic master template was generated using a rapid prototyping instrument and a schematic drawn in Google Sketchup 8. The template was filled with Silastic T2, degassed, and cured at 70 °C. Once the silicone pillar array was removed from the template, it was affixed to an airfoil which was placed into a bench top wind tunnel that had a maximum airflow of approximately 13 m/s (Figure 10A). At this wind speed no pillar deflection was detected. A turbulent jet was introduced using compressed air which generated air speeds from 30 to 90 m/s. Under these conditions, pillar deflection was readily visible. Using high speed photography (a Phantom V12 camera operating at 5000 frames/s), the pillar motions could be observed (Figure 10B and C). Although there is significant fluctuation due to the turbulence of the airflow, the motion of the silicone pillars is consistent with their relative positions on the airfoil.

National Aeronautics and Space Administration
Langley Research Center Hampton, Virginia 23681-2199

October 2013

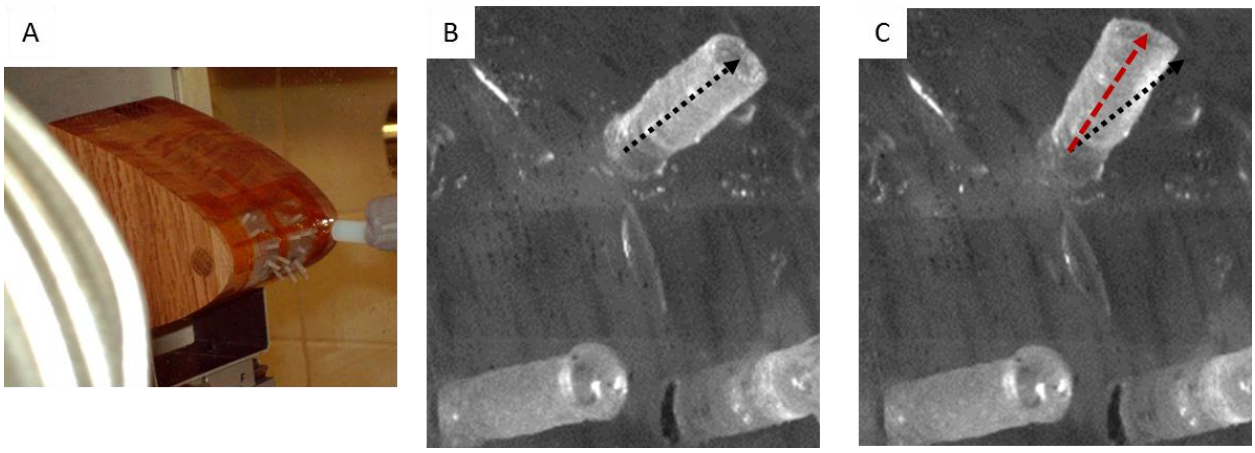

Figure 10. (A) Macroscale pillar sample mounted on an airfoil in a benchtop wind tunnel. The turbulent jet source is the white tubing located in the middle right portion of the picture. High speed photography was taken before (B) and after (C) the turbulent jet was turned on. With an air pressure of 25 psi, the pillar shown in figures 8B and C was observed to deflect approximately 18°.

The current TRL of this technology is estimated to be 2-3.

Outlook and Future Work

Before implementation of these micropillar arrays as a sensor in a wind tunnel experiment can be completed, several additional experiments need to be conducted to determine the repeatability of micropillar fabrication, the similarity in response to force of pillar deflection, pillar deflection variations in an array relative to a single pillar, among many others. Beyond this, the utility of these surfaces as sensors needs to be evaluated including the sensor bandwidth, frequency response, noise floor, etc. Determination of the micropillar frequency response range and fundamental frequencies would need to be determined using simple cantilever deflection calculations. Verification of these calculations could be performed using deflection experiments and high speed imaging. The development of simple models in programming platforms such as COMSOL would also aid in addressing several issues yet to be addressed including deformation of the pillar caps and changes in response to shear stress as a result of deflection of the capped pillar.

Additionally, signal transduction methods will need to be investigated. One of the most promising approaches appears to be optical detection. Deflection of the micropillar shear stress sensor components may be visualized using existing wind tunnel technologies involved with particle image velocimetry, specifically μ-PIV systems.[26] Using state-of-the-art μ-PIV systems, imaging at micrometer per pixel levels and lower is achievable. Thus a 100 μm pillar with a deflection of 20 μm should have a change in position of at least 20 pixels in a single direction. A 20 μm diameter with a 50 μm 'cap' would occupy 2032 pixels. With the large 'caps' resolutions much better than 0.01 pixels should be achievable.

National Aeronautics and Space Administration
Langley Research Center Hampton, Virginia 23681-2199

Acknowledgements

The authors would like to acknowledge Vincent Cruz (NASA Langley Research Center) for assistance with contact lithography processes. The authors would also like to acknowledge Dr. Mark Sheplak (University of Florida) for technical discussions. Funding for this research was provided by the NASA ARMD NARI (NASA Aeronautics Research Institute) Seedling program.

References

1. Dijkstra, M.; van Baar, J. J.; Wiegerink, R. J.; Lammerink, T. S. J.; de Boer, J. H.; Krijnen, G. J. M., Artificial Sensory Hairs Based on the Flow Sensitive Receptor Hairs of Crickets. *Journal of Micromechanics and Microengineering* **2005,** *15*, S132-S138.
2. Naughton, J. W.; Sheplak, M., Modern developments in shear-stress measurement. *Progress in Aerospace Sciences* **2002,** *38*, 515-570.
3. Lofdahl, L.; Gad-el-Hak, M., MEMS-Based Pressure and Shear Sensors for Turbulent Flows. *Measurement Science and Technology* **1999,** *10* (8), 665-686.
4. Meloy, J.; Griffin, J.; Sells, J.; Chandrasekaran, V.; Cattafesta, L.; Sheplak, M., Experimental Verification of a MEMS Based Skin Friction Sensor for Quantitative Wall Shear Stress Measurement. In *41st AIAA Fluid Dynamics Conference and Exhibit*, Honolulu, Hawaii, 2011.
5. Ioppolo, T.; Ayaz, U. K.; Otugen, M. V., Performance of a Micro-Optical Wall Shear Stress Sensor Based on Whispering Gallery Mode Resonators. In *47th AIAA Aerospace Sciences Meeting*, American Institute of Aeronautics and Astronautics, Inc.: Orlando, FL, 2009.
6. Brucker, C.; Spatz, J.; Schroder, W., Feasability Study of Wall Shear Stress Imaging using Microstructured Surfaces wuth Flexible Micropillars. *Experiments in Fluids* **2005,** *39*, 464-474.
7. Grobe, S.; Schroder, W.; Brucker, C., Nano-Newton Drag Sensor Based on Flexible Micro-Pillars. *Measurement Science and Technology* **2006,** *17*, 2689-2697.
8. Schmitz, G. J.; Brucker, C.; Jacobs, P., Manufacture of High-Aspect-Ratio Micro-Hair Sensor Arrays. *Journal of Micromechanics and Microengineering* **2005,** *15*, 1904-1910.
9. Grobe, S.; Schroder, W., Mean Wall-Shear Stress Measurements Using the Micropillar Shear-Stress Sensor MPS3. *Measurement Science and Technology* **2008,** *19*, 015403.
10. Grobe, S.; Schroder, W., Dynamic Wall-Shear Stress Measurements in Turbulent Pipe Flow Using Micro-Pillar Sensors MPS3. *International Journal of Heat and Fluid Flow* **2008,** *29*, 830-840.
11. Notterbrock, B.; Klaas, M.; Schroder, W., Improvement of the Measurement Range of the Micro-Pillar Shear-Stress Sensor MPS3. In *28th AIAA Aerodynamic Measurement Technology, Ground Testing, and Flight Testing Conference*, New Orleans, Louisiana, 2012.
12. (a) Autumn, K.; Liang, Y. A.; Hsieh, S. T.; Zesch, W.; Chan, W. P.; Kenny, T. W.; Fearing, R.; Full, R. J., Adhesive Force of a Single Gecko Foot-Hair. *Nature* **2000,** *405*, 681-685; (b) Geim, A. K.; Dubonos, S. V.; Grigorieva, I. V.; Novoselov, K. S.; Zhukov, A. A.; Shapoval, S. Y., Microfabricated Adhesive Mimicking Gecko Foot-Hair. *Nature Materials* **2003,** *2*, 461-463.
13. Tuteja, A.; Choi, W.; Ma, M.; Mabry, J. M.; Mazzella, S. A.; Rutledge, G. C.; McKinley, G. H.; Cohen, R. E., Designing Superoleophobic Surfaces. *Science* **2007,** *318*, 1618-1622.
14. (a) Oner, D.; McCarthy, T. J., Ultrahydrophobic surfaces. Effects of topography length scales and wettability. *Langmuir* **2000,** *16*, 7777 - 7782; (b) Callies, M.; Chen, Y.; Marty, F.; Pepin, A.; Quere, D., Microfabricated textured surfaces for superhydrophobic investigations. *Microelectronics Engineering* **2005,** *78-79*, 100 - 105.

National Aeronautics and Space Administration
Langley Research Center Hampton, Virginia 23681-2199

October 2013

15. del Campo, A.; Greiner, C.; Arzt, E., Contact shape controls adhesion of bioinspired fibrillar surfaces. *Langmuir* **2007,** *23*, 10235 - 10243.
16. Rajput, D.; Costa, L.; Lansford, K.; Terekhov, A.; Hofmeister, W., Solution-Cast High-Aspect-Ratio Polymer Structures from Direct-Write Templates. *ACS Appl. Mater. Interfaces* **2013,** *5*, 1-5.
17. (a) Kapadia, R.; Ko, H.; Chueh, Y.-L.; Ho, J. C.; Takahashi, T.; Zhang, Z.; Javey, A., Hybrid Core-Multishell Nanowire Forests for Electrical Connector Applications. *Applied Physics Letters* **2009,** *94*, 263110; (b) Gnanamanickam, E. P.; Sullivan, J. P., Manufacture of High Aspect Ratio Micro-Pillar Wall Shear Stress Sensor Arrays. *Journal of Micromechanics and Microengineering* **2012,** *22*, 125015.
18. Chandra, D.; Yang, S., Stability of High-Aspect-Ratio Micropillar Arrays against Adhesive and Capillary Forces. *Accounts of Chemical Research* **2010,** *43* (8), 1080-1091.
19. Grobe, S.; Schroder, W., The Micro-Pillar Shear-Stress Sensor MPS3 for Turbulent Flow. *Sensors* **2009,** *9*, 2222-2251.
20. (a) Wohl, C. J.; Belcher, M. A.; Chen, L.; Connell, J. W., Laser Ablative Patterning of Copoly(imide siloxane)s Generating Superhydrophobic Surfaces. *Langmuir* **2010,** *26* (13), 11469-11478; (b) Belcher, M.; Wohl, C.; Hopkins, J.; Connell, J., Laser Surface Preparation for Bonding of Aerospace Composites. *Engineering and Computational Mechanics* **2011,** *164* (3), 133-138.
21. Song, J.; Wang, X.; Riedo, E.; Wang, Z., Elastic Propertyof Vertically Aligned Nanowires. *Nano Letters* **2005,** *5* (10), 1954-1958.
22. Kallesoe, C.; Larsen, M. B.; Boggild, P.; Molhave, K., 3D Mechanical Measurements with an Atomic Force Microscope on 1D Structures. *Review of Scientific Instruments* **2012,** *83*, 023704.
23. Gordon, M. J.; Baron, T.; Dhalluin, F.; Gentile, P.; Ferret, P., Size Effects in Mechanical Deformation and Fracture of Cantilevered Silicon Nanowires. *Nano Letters* **2009,** *9* (2), 525-529.
24. McFarland, A. W.; Poggi, M. A.; Bottomley, L. A.; Colton, J. S., Characterization of microcantilevers solely by frequency response acquisition. *Journal of Micromechanics and Microengineering* **2005,** *15*, 785-791.
25. (a) Wiesenborn, A. J.; Mazur, P., The Oseen Drag on a Circular Cylinder Revisited. *Physica A: Statistical Mechanics and its Applications* **1984,** *123* (1), 191-208; (b) Deen, W., M., *Analysis of Transport Phenomena*. New York, 1998; p 597.
26. Raffel, M.; Willert, C.; Kompenhans, J., *Particle Image Velocimetry: A Practical Guide (Experimental Fluid Mechanics)*. 2nd Edition ed.; Springer: Berlin, Germany, 2007; p 448.

National Aeronautics and Space Administration
Langley Research Center Hampton, Virginia 23681-2199

October 2013

Appendix A. Approximation of Shear Stress on a Surface Based on AFM Derived Forces of a PDMS Micropillar

The force on a micropillar was measured using AFM cantilever with 3 μm of deflection. The force required to deflect the post to 10% of the pillar height can be extrapolated from that information. This force must be equivalent to an applied drag force acting on a pillar of the same dimensions. An order of magnitude approximation can be made by assuming the cylinder is infinitely long and is in a uniform Stokes flow. The velocity of the flow field far from the cylinder can be calculated from the drag equation which accounts for skin friction and form drag. Using this velocity, the average velocity in a flow field near a surface can be estimated from the definition of Newtonian shear stress.

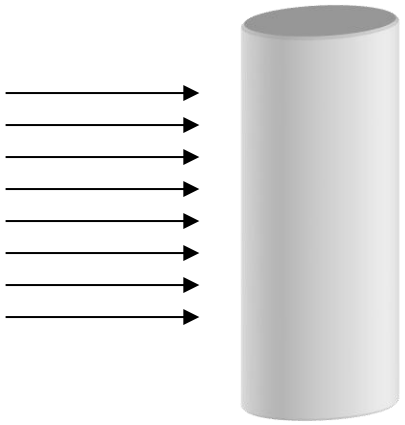

Figure 1: Schematic of velocity vectors acting on an infinite cylinder in a Stokes flow.

The spring constant (k) of an elastomeric pillar can be modeled using Hooke's Law (Eq. 1) for an ideal spring to determine the relationship between force (F) and deflection (y) of the pillar. For shear stress measurement, fluid drag on the pillar induces parasitic drag force (F_D) on a pillar which induces a deflection in accordance with Hooke's Law.

$$F_D = F = ky \tag{1}$$

The parasitic drag can be calculated for a bluff body using the drag equation, Eq. 2:

$$F_D = \frac{1}{2}\rho \upsilon^2 C_D A \tag{2}$$

National Aeronautics and Space Administration
Langley Research Center Hampton, Virginia 23681-2199

October 2013

where the density (ρ), the drag coefficient (C_D), and the frontal area of a pillar (A) are constants that are known for a given flow and cylinder geometry. The drag coefficient for an infinite, circular cylinder in Stokes flow is Reynolds number, *Re*, dependent and is available from literature sources. Because *Re* is dependent on ν, the values of *Re* and C_D are iteratively calculated until the solution converges (less than 1% variation).

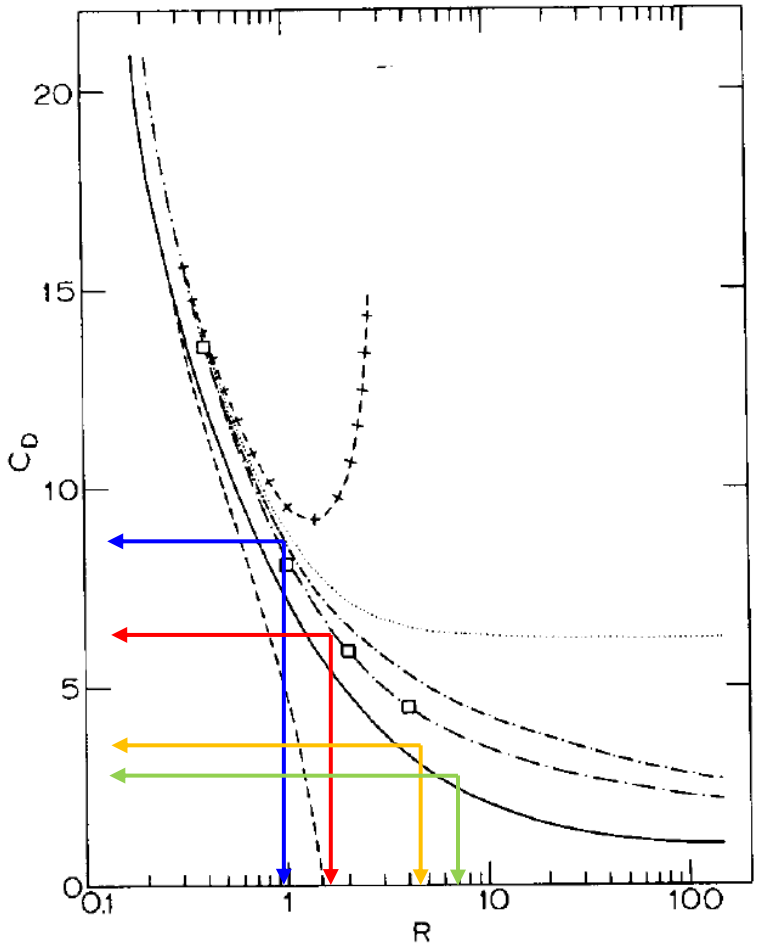

Figure 2: Coefficient of drag for an infinite cylinder in Stokes Flow. The solid line represents experimental data. Other curves are generated for analytical approximations. Copied from: *Weizenborn A.J. and Mazur P. Physica 123A (1984) 191-208 North-Holland, Amsterdam.*

The following table shows values for convergent solutions of the drag equation for four cases where the applied drag forces are similar to those applied during micropillar calibration experiments using an AFM. For each force level a set of C_D and *Re* values are indicated on the graph in Figure 2.

National Aeronautics and Space Administration
Langley Research Center Hampton, Virginia 23681-2199

The shear stress imparted on a surface by a flowing Newtonian fluid is defined as:

$$\tau = \mu \frac{\delta U}{\delta z} \tag{3}$$

where τ is the shear stress, μ is the dynamic viscosity, and z is the distance from the surface. For this approximation, the velocity of a uniform flow field past an infinite cylinder is assumed to equal the average velocity of gradient flow field in the boundary layer above a surface. The figure below represents this graphically (Figure 3).

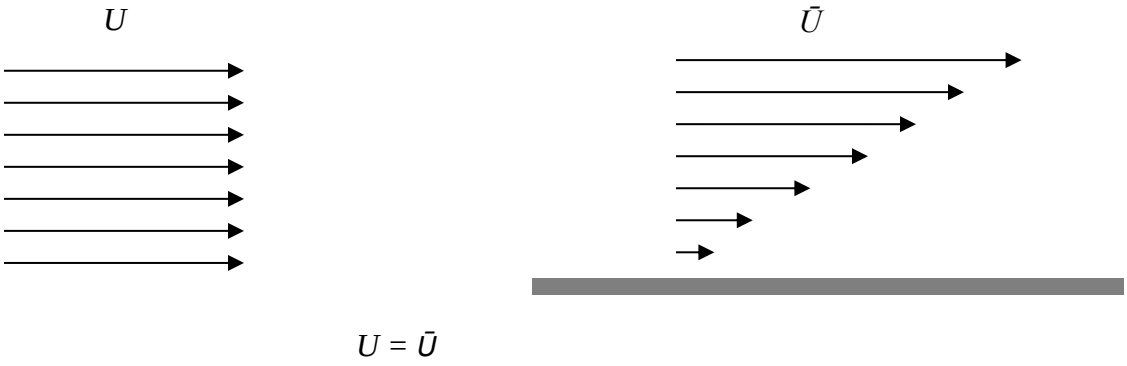

Figure 3: Schematic of the change in the velocity profile from the free stream, left, to that in the boundary layer with a no-slip condition, right.

Using this assumption, the velocity of the flow for each the four cases in the table can be used to calculate the resulting shear stress on a flat surface. Within the viscous sublayer, the flow field can be assumed to vary linearly with distance from the surface so the shear stress can be calculated using Eq. 4:

$$\tau = \mu \frac{\Delta U}{\Delta z} \tag{4}$$

Where the change in velocity (ΔU) is twice the average velocity and the change is height (Δz) is the length of the pillar. The results of this calculation are included in table 1.

Table 1. Calculated shear forces for given pillar deflection force, drag coefficients, and Reynold's numbers.

Force, nN	C_D	Re	Line Color, Figure 2	τ, mPa
100	3.0	5.3	green	823
50	3.6	3.4	orange	517
10	6.5	1.1	red	176
5	8.0	0.7	blue	112

National Aeronautics and Space Administration
Langley Research Center Hampton, Virginia 23681-2199

October 2013